



LAWRENCE
LIVERMORE
NATIONAL
LABORATORY

Air Blasts from Cased and Uncased Explosives

L. A. Glenn

April 12, 2016

Disclaimer

This document was prepared as an account of work sponsored by an agency of the United States government. Neither the United States government nor Lawrence Livermore National Security, LLC, nor any of their employees makes any warranty, expressed or implied, or assumes any legal liability or responsibility for the accuracy, completeness, or usefulness of any information, apparatus, product, or process disclosed, or represents that its use would not infringe privately owned rights. Reference herein to any specific commercial product, process, or service by trade name, trademark, manufacturer, or otherwise does not necessarily constitute or imply its endorsement, recommendation, or favoring by the United States government or Lawrence Livermore National Security, LLC. The views and opinions of authors expressed herein do not necessarily state or reflect those of the United States government or Lawrence Livermore National Security, LLC, and shall not be used for advertising or product endorsement purposes.

This work performed under the auspices of the U.S. Department of Energy by Lawrence Livermore National Laboratory under Contract DE-AC52-07NA27344.

Air Blasts from Cased and Uncased Explosives

L. A. Glenn

April 4, 2016

Abstract:

The problem of a spherical blast in air is solved using the STUN code. For bare charges, the calculations are shown to be in excellent agreement with previous published results. It is demonstrated that, for an unconfined (uncased) chemical explosive, both range and time to effect scale inversely as the cube root of the yield and directly as the cube root of the ambient air density. It is shown that the peak overpressure decays to roughly 1/10 of ambient pressure in a scaled range of roughly $10 \text{ m/kg}^{1/3}$ at sea level. At a height of 30 km, where the ambient density is a factor of 64 less, the range to the same decay increases to $40 \text{ m/kg}^{1/3}$. As a direct result of the scaling a single calculation suffices for all charge sizes and altitudes. Although the close-in results are sensitive to the nature of the explosive source and the equation of state of the air, this sensitivity is shown to virtually disappear at scaled ranges $> 0.5 \text{ m/kg}^{1/3}$.

For cased explosives the case thickness introduces an additional scale factor. Moreover, when the blast wave arrives at the inner case radius the case begins to expand. Fracture occurs when a critical value of the resulting hoop strain is reached, causing the case to shatter into fragments. A model is proposed to describe the size distribution of the fragments and their subsequent motion via drag interaction with the explosion products and ambient air. It is shown that a significant fraction of the charge energy is initially transmitted to the case fragments in the form of kinetic energy; for example, a 1 kg spherical charge with a 5 mm thick steel case has almost 29% of the total charge energy as initial kinetic energy of case fragments. This percentage increases with increasing case thickness and decreases with increasing charge size. The peak overpressure at a given range is 70-85% for cased explosives as compared with uncased and the peak impulse per unit area is 90-95%. The peak overpressure and impulse also decrease rapidly with altitude.

The effect of the fragments is to increase lethality. Whereas at a scaled range of $10 \text{ m/kg}^{1/3}$, the peak overpressure is an order of magnitude less than the ambient pressure, the number of fragments per unit area is close to $1 \text{ m}^{-2}/\text{kg}^{1/3}$, independent of case thickness or altitude. For sufficient ratio of case-to-explosive mass, the number of fragments scales with the cube root of the yield and is independent of case thickness.

1.0 Introduction

The problem of a spherical blast in air has been solved analytically for strong shocks in an ideal gas (*von Neumann 1944*) and in the weak shock approximation (*Bethe 1944*). For intermediate regions it has been found necessary to resort to numerical methods. The first such comprehensive study was carried out for an ideal gas (*Brode 1955*) and then extended to include a real air equation of state (*Brode 1956*). The STUN code (*Glenn 2001*) was developed to simulate nuclear explosions in tunnels and consists of a spherical component to model the early stages of the explosion coupled to an axial component that handles the flow through the tunnel complex; if the tunnel diameter is set to an arbitrarily large value no source code modifications are required to deal with uncased spherical blasts. STUN can also handle explosive charges in which inert particles are embedded either within or on the charge periphery (*Glenn and Lomov 2012*).

In what follows we present the results of a brief study of explosions at arbitrary altitude with the STUN code. We begin by focusing on bare charges and the scaling law that applies in that case. Next we examine the chronology that obtains when the blast wave arrives at a case surrounding the charge. The fracture that occurs when the case expands beyond a critical point results in a process of fragmentation and a model is proposed to describe the size distribution of the fragments and their subsequent motion due to drag interaction with the explosion products and surrounding air. Calculations are then performed to exhibit the differences in peak overpressure, impulse, and the effect of the fragments.

2.0 Analysis

2.1 Bare Charges

The scaling law for explosions is based on the principles of geometric similarity and conservation of momentum. Although it is possible to express the scaling in non-dimensional form, the following will be more convenient for our purposes:

$$\bar{R} = R(\rho_{amb} / \rho_0 W)^{1/3} \quad (1)$$

and

$$\bar{t} = t(\rho_{amb} / \rho_0 W)^{1/3} \quad (2)$$

where R is the range from the center of the explosive, ρ_{amb} is the ambient air density, ρ_0 is the ambient air density at sea level, and W is the explosive yield. Figures 1 and 2 exemplify how the overpressure scales with both \bar{R} and \bar{t} . Figure 1 depicts the dynamic overpressure ratio, $(P_{dy} - P_{amb}) / P_{amb}$, as a function of \bar{t} at a fixed value of $\bar{R} = 1 \text{ m/kg}^{1/3}$. $P_{dy} = P + (1/2)\rho u^2$ and u is the local velocity. Three separate calculations are shown in the figure. All 3 were run with C4 explosive using the JWL equation of state (*Lee et al. 1968*) and assuming air to be described as an ideal gas with $\gamma = 1.4$. The reference blue

curve was run with a yield of 1 kg and ambient density 1 bar (sea level) and displays the overpressure ratio at a range of 1 m. The same ambient density obtains for the red curve but the yield was increased by a factor of 8; to maintain \bar{R} at $1 \text{ m/kg}^{1/3}$ requires the overpressure to be displayed at a range of 2 m in this case. Finally, the gold curve refers to a calculation in which the yield was set at 8 kg but the ambient density was decreased by a factor of 8. In this case, to maintain \bar{R} at $1 \text{ m/kg}^{1/3}$ requires the overpressure to be displayed at a range of 4 m. It is observed that all three curves are congruent in the figure.

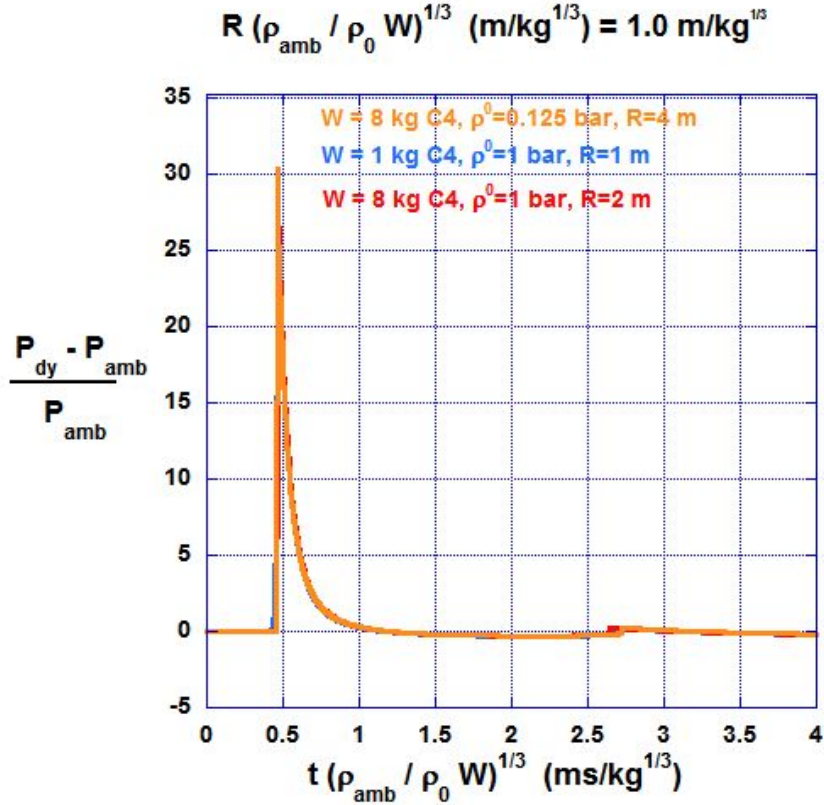


Fig. 1 Dynamic overpressure ratio as a function of scaled time at a scaled range of $1 \text{ m/kg}^{1/3}$.

Similarly, figure 2 shows the dynamic overpressure at a scaled range of $10 \text{ m/kg}^{1/3}$. In this case, four separate calculations are shown to overlay, where we have included the case where both the charge size and the ambient density have been reduced by a factor of 125. It is therefore clear that, as long as the ambient density remains invariant over the field of interest, a single calculation suffices to describe the result for any value of W and ρ_{amb} . The assumption of invariant ρ_{amb} will be further justified below.

Figure 3 displays the peak overpressure ratio as a function of scaled range. The open circles show the STUN results, both static and dynamic for $0.5 \leq \bar{R} \leq 10 \text{ m/kg}^{1/3}$. Also shown in the figure are Brode's (1956) results for a TNT energy source with a real gas approximation for the equation of state of air.

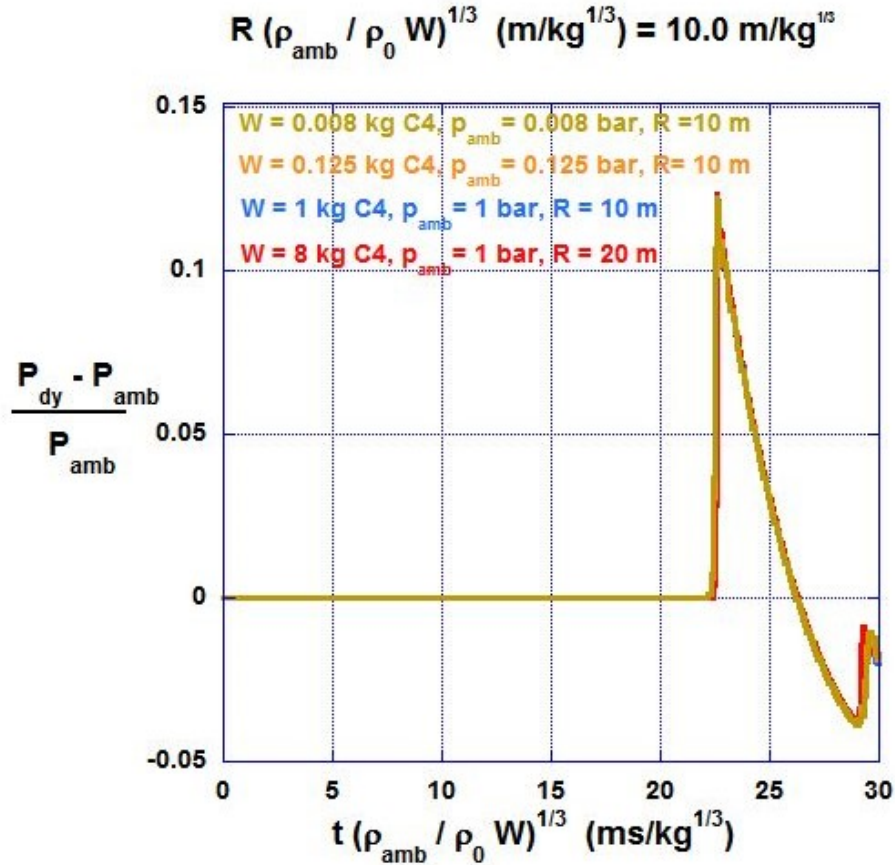


Fig. 2 Dynamic overpressure ratio as a function of scaled time at a scaled range of $10 \text{ m/kg}^{1/3}$.

It can be seen that the latter results are in excellent agreement with the STUN calculations, suggesting that the assumption of an ideal gas description for the air is justified. We note, however, that at scaled range $< 0.5 \text{ m/kg}^{1/3}$ (not shown in figure 3), Brode found very substantial differences between the calculations with real and ideal gas air. This, of course, is to be expected because closer to the explosion source the elevated temperatures cause dissociation and ionization which are not accounted for in the ideal gas model. It should also be noted that the scaled range at which the ideal gas approximation for air is appropriate would be much greater in the case of a nuclear explosion where the thermal reach is substantially further than with chemical explosives.

Figure 4 compares the scaled time of arrival of the shock front as computed by Brode with the results obtained with STUN. Again, the results are seen to be in excellent agreement.

Finally, as noted above, the scaling enables a single calculation to describe the result for any yield and ambient density as long as the latter remains invariant over the field of interest. If the latter is assumed to be defined by the peak overpressure decaying to 1/10 of the ambient air pressure, then figure 3 shows that this occurs at roughly $\bar{R} = 10 \text{ m/kg}^{1/3}$.

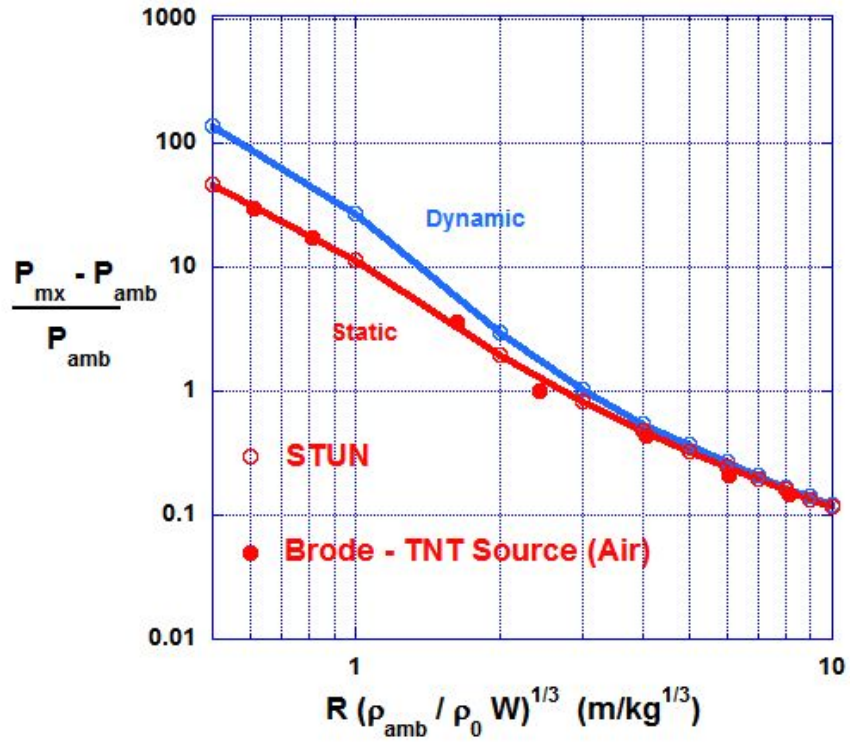


Fig. 3 Peak overpressure ratio as a function of scaled range.

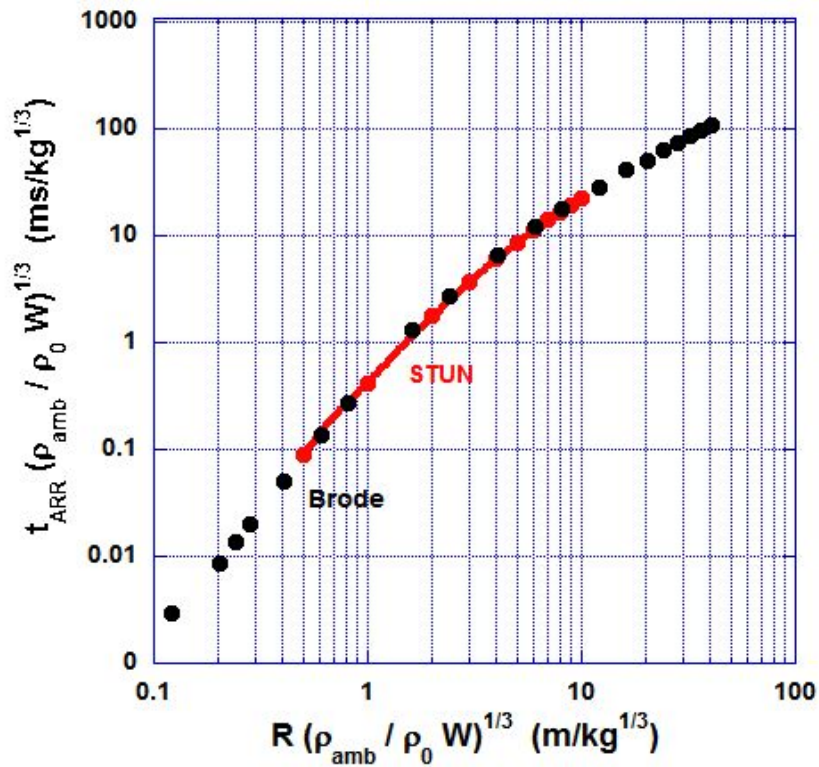


Fig. 4 Scaled time of arrival of shock front.

Typical missile warheads range from ~4 kg for air-to-air combat (Sidewinder) to as much as 90 kg for ground-to-air (Patriot). So, at sea level, the field of interest would extend from $10(4)^{1/3} = 15.9$ m to $10(90)^{1/3} = 44.8$ m. Figure 5 depicts the standard model ambient air density from a height of 10 m above sea level to a height of 30 km. For a 50 m change in elevation at the 10 m level the change in density is less than 1%. By contrast, at the 30 km level the ambient density is a factor of 64 times less than at sea level so the field of interest is 4 times greater than an sea level or as much as 180 m for a 90 kg charge. At the 30 km level, a change in elevation of 180 m leads to an ambient air density change of 3.2%. It thus appears that the assumption of uniform ambient density over the range of interest is well justified.

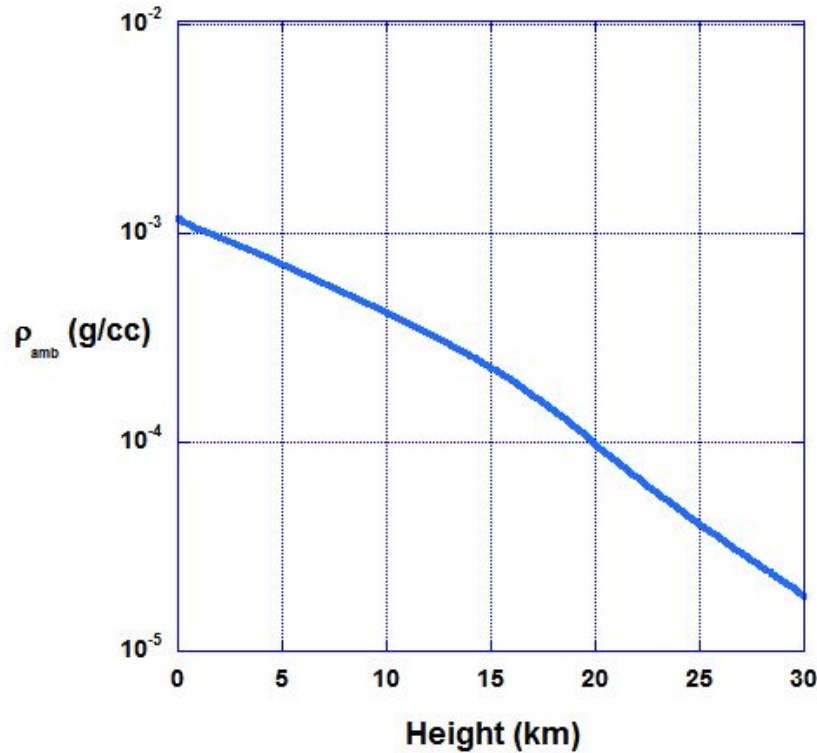


Fig. 5 Ambient air density as a function of height above sea level.

2.2 Cased Charges

2.2.1 Size distribution of fragments

A theoretical understanding of dynamic fragmentation requires a satisfactory statistical, as well as physical, explanation. Even in situations of perfect symmetry, such as the rapid expansion of a spherical shell considered here, the process of breakup is random leading to a distribution in fragment size and shape. A substantial literature exists in which the statistical and physical principles underlying the processes of dynamic fragmentation have been explored. The basic idea first proposed (*Mott 1943*) was to extend the geometric concept of random points on a line to the random fragmentation of a two-

dimensional region or area by considering the distribution in fragment areas that occurs from the random distribution of horizontal and vertical lines of equal density on an infinite area. This simple concept was shown to lead directly to a distribution relating the cumulative number of fragments and the fragment mass. This distribution had considerable success in providing a description of exploding munitions data although empirical generalization of the Mott expression was often necessary. The method proposed by Mott is, however, only one way in which to randomly fragment an area; there are many ways in which straight or curvilinear lines or line segments can be randomly distributed to fragment an area. And these other methods lead to distributions that differ from Mott.

A different method for randomly partitioning an area is one that avoids the selection of a particular geometric description (*Grady and Kipp 1985*). If the fragment area is viewed as a scalar variable, fragmentation is determined by breaks distributed randomly on the scalar measure of area. These points define a Poisson variate and lead to a cumulate fragment distribution of the form:

$$N(a) = N_0 e^{-N_0 a} \quad (3)$$

where N_0 is the number of fragments per unit area and a is the fragment area. This linear exponential distribution is in contrast with the Mott result in which the argument of the exponential depends on the square root of the fragment area. It can be shown that certain methods for geometrically fragmenting an area are in close agreement with the linear exponential distribution.

Still other geometric constructions are possible. A fairly recent review of 7 of these, in which both the Mott and Grady distributions were included, tested the results against experimental data from 30 fragmenting projectiles (*Elek and Jaramaz 2007*). It was found that the Grady distribution, or an extended version thereof, produced the best results. Accordingly, this is the distribution employed here.

Figure 6 shows the cumulative fragment mass distribution derived by Grady:

$$M(m / \bar{m}) = (1 + m / \bar{m}) e^{-m / \bar{m}} \quad (4)$$

where $M = M_T / M_0$, M_T is the cumulative fragment mass, M_0 is the total mass of fragments (case mass), m is the individual fragment mass, and \bar{m} is the average individual fragment mass.

If we limit the domain to the region $0 \leq m / \bar{m} \leq 6$ in figure 6, and subdivide this domain into n segments, the fraction of the case mass in segment k is simply $\Delta M(k) = M(k+1) - M(k)$ and we renormalize such that $\sum_{k=1}^n \Delta M(k) = 1$. Figure 7 shows the fraction of case mass for each of 10 fragment mass segments ($n = 10$). The total number of fragments is then simply

$$N_T = M_0 \sum_{k=1}^n \Delta M(k) / m(k). \quad (5)$$

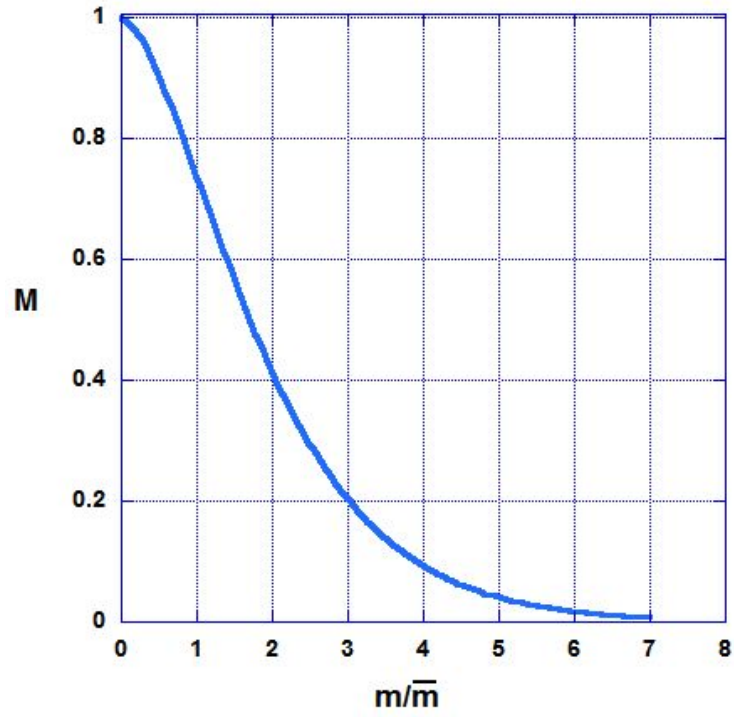


Fig. 6 Grady cumulative fragment mass distribution.

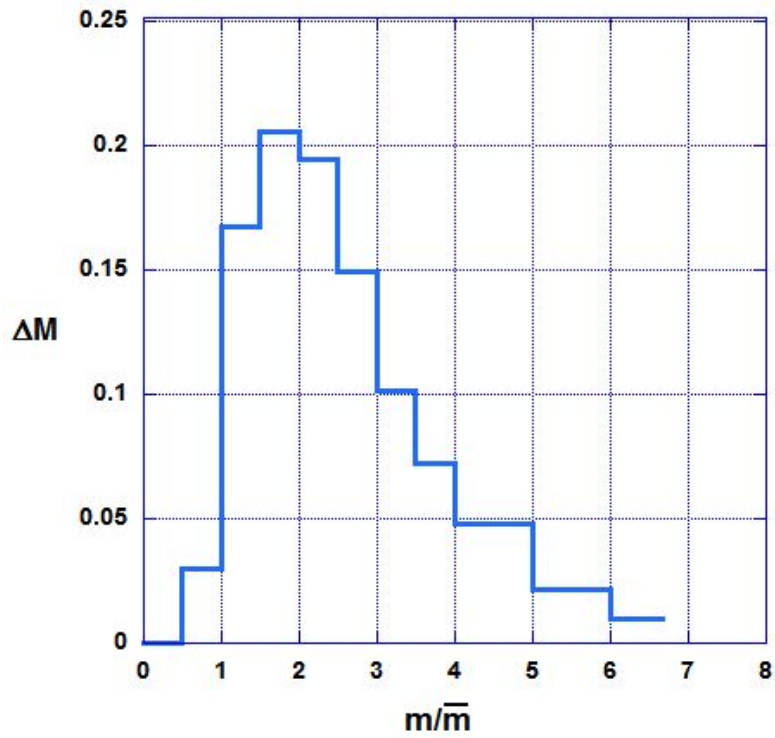


Fig. 7 Fraction of case mass as a function of fragment mass derived from Grady cumulative fragment distribution.

2.2.2 Average fragment size

Statistical geometry allows for insight into the distribution of fragment sizes but only expressed in terms of the average fragment mass, \bar{m} . The latter must be determined based on physical grounds. If the case is assumed to be made of ductile material, i.e., experiences significant plastic strain prior to fracture, then it can be shown that the average fragment size is determined by balancing the local kinetic energy, the fragment surface energy (which is created during the formation of new fragment surface area) and the stored elastic (strain) energy (*Glenn and Chudnovsky 1986*). The local kinetic energy measures the intensity of expansion of the case and is responsible for driving the fragmentation process. A crucial point is the recognition that the total kinetic energy of the case is not available for fragmentation. Only that fraction that is relative to the center of mass can participate in the breakage, while the remainder must continue to reside in the rigid body flight of fragments.

The result of applying the energy balance leads to the following equation for the average fragment equivalent diameter:

$$\bar{d}_f = 2 \left[5 (K_{Ic} / \rho c \dot{\epsilon})^2 \right]^{1/3} \quad (6)$$

where $K_{Ic} = \sqrt{2\rho c^2 \gamma}$ is the fracture toughness, ρ is the case density, c the bulk sound speed, $\dot{\epsilon}$ is the (hoop) strain rate $= U / R_0$, U is the case velocity, R_0 is the initial case radius, and γ the surface energy. And of course, $\bar{m} = \pi \bar{d}_f^3 / 6$.

Equation (6) is in good agreement with explosive fragmentation of high-strength steels that are typically employed as explosive casings (*Weimer and Rogers 1979*). On the other hand, for a truly brittle material, with low fracture toughness and high fracture initiation stress, the fragment size has been found to be independent of strain rate and, from linear elastic fracture mechanics, proportional to the square of the ratio of the fracture toughness to the initiation stress (*Glenn, Gommerstadt and Chudnovsky 1986*):

$$\bar{d}_f = 2 \left((1 - \nu^2 / 1 - 2\nu) (K_{Ic} / \sigma_*)^2 \right) \quad (7)$$

Figure 8 displays equations 6 and 7 with data for AISI 4340 steel, also commonly used as a case material (*Ritchie et al. 1976*).

Figure 9 show the results of STUN calculations with AISI 4340 steel for strain rate as a function of strain prior to the onset of fracture for two charge sizes, 1 kg and 8 kg, and for two case thicknesses, 2.5 mm and 5 mm. The experimental data indicate a minimum strain to fracture, ϵ_{cr} , of $\sim 5\%$ although this quantity depends apparently on the austenizing temperature and the value could be significantly higher. The critical strain rate (in equation (6)) is seen to decrease with increasing charge size and with increasing case thickness.

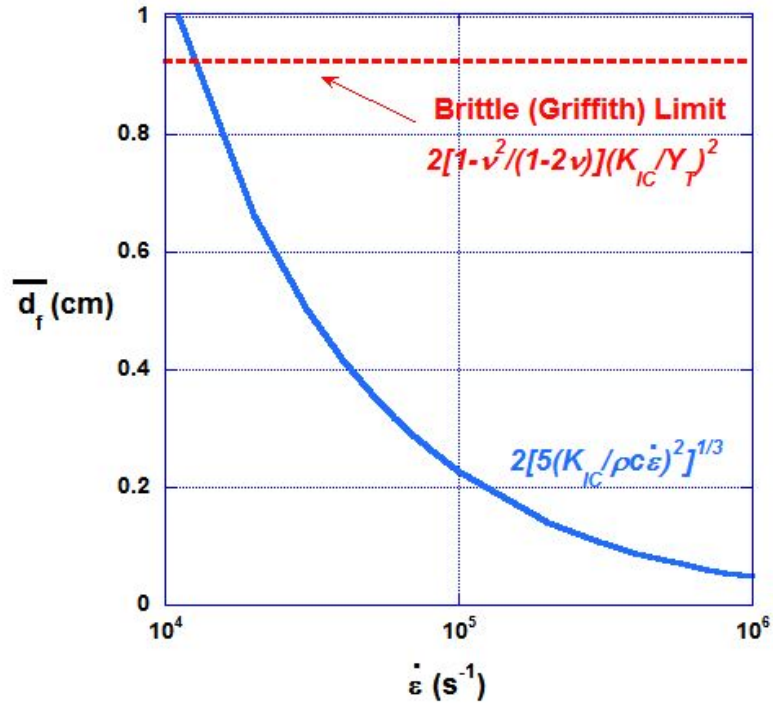


Fig. 8 Average fragment equivalent diameter as a function of strain rate.

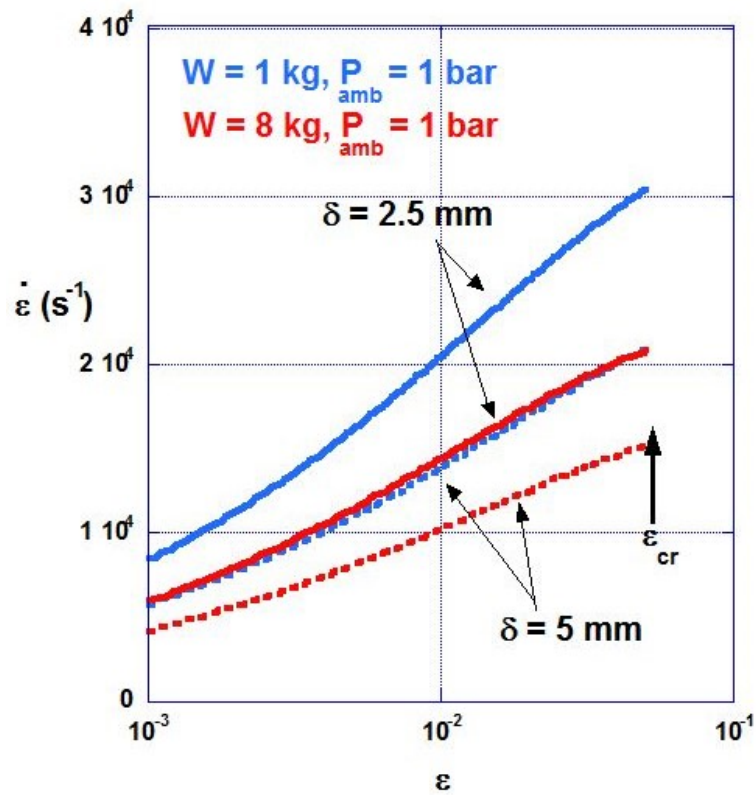


Fig. 9 Strain rate at the onset of fracture for AISI 4340 steel.

2.2.3 Fragment motion

Once the case has shattered the initial velocity of the fragments will be that of the case just prior to fracture and their subsequent motion will be governed by drag interaction with the explosion products and eventually with the surrounding air. The initial volume fraction of the fragments will approach unity at the instant of fracture but will rapidly decrease as the fragments expand into the surrounding air. The drag coefficient for such a system was derived by *Smirnov (1988)* and validated by *Ripley (2010)*:

$$c_D = \begin{cases} C_1 = \frac{24}{Re} + \frac{44}{Re^{0.5}} + 0.42 & \phi_f \leq 0.08 \\ C_2 = \frac{4}{3(1-\phi_f)} \left(\frac{7}{4} + \frac{150\phi_f}{(1-\phi_f)Re} \right) & \phi_f \geq 0.45 \\ \frac{(\phi_f - 0.08)C_2 + (0.45 - \phi_f)C_1}{0.37} & 0.08 < \phi_f < 0.45 \end{cases} \quad (8)$$

Here ϕ_f is the fragment volume fraction and Re is the Reynolds number based on the fragment equivalent diameter and velocity relative to the surrounding medium; an additional correction was made for the Mach number but this was insignificant. The drag coefficient obtained from equation (8) can be an order of magnitude higher when the fragment volume fraction approaches unity than when the fragments are highly diluted.

3.0 Results

3.1 Fragment velocity

Figure 10 shows the velocity of the various fragment mass segments as a function of range for a 1 kg charge with 2.5 mm case thickness at sea level. In this and subsequent figures the case is made of AISI 4340 steel. The case attained a velocity just prior to fracture of 1.65 km/s. It is observed that the smallest diameter (mass) fragments (3.98 mm in this instance) then initially accelerated the fastest, quickly achieving a peak velocity of 1.93 km/s, but then were more rapidly decelerated by the surrounding air than the larger fragments; at 40 m range the smallest fragments had their velocity reduced to only 0.73 km/s. By contrast, the largest diameter fragments (9.11 mm) initially reached a peak velocity of 1.83 km/s but were decelerated more slowly and at 40 m range still were traveling at 1.21 km/s. The deceleration phase began almost immediately after breakthrough of the explosion products as the fragments encountered the more slowly moving ambient air. It will be seen below that when the same charge and case thickness is employed at 30 km altitude there is practically no deceleration of any of the fragment segments because the drag force of the surrounding air, with an ambient density only 1/64th that of sea level, is very much diminished.

Figure 11 is similar to figure 10 except that in this instance the case thickness is increased from 2.5 mm to 5 mm. The behavior of the fragment mass segments is similar. The smallest fragments here have

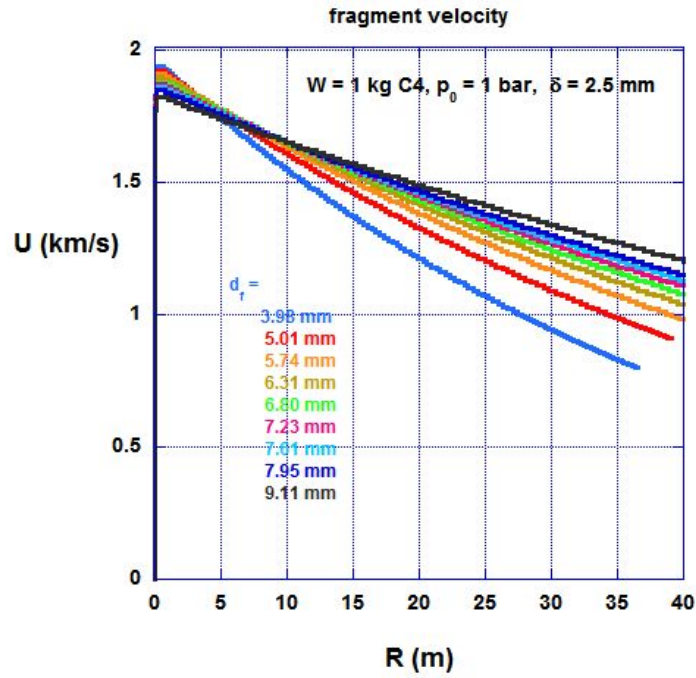


Fig. 10 Fragment velocity for 1 kg charge and 2.5 mm case thickness at sea level.

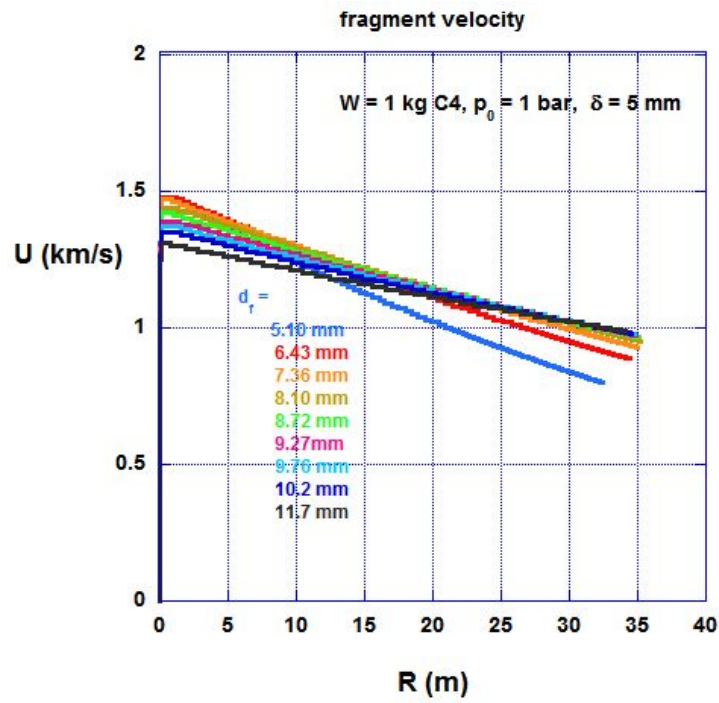


Fig. 11 Fragment velocity for 1 kg charge and 5 mm case thickness at sea level.

diameter 5.10 mm and the largest 11.7 mm and their velocity trajectories are significantly reduced as compared with the 2.5 mm case thickness. The case velocity just prior to fracture in this instance was only 1.17 km/s and the 5.10 mm diameter fragments were then accelerated to a peak velocity of 1.48 km/s but then were decelerated to roughly the same level as with the thinner case at 40 m range. Comparing figure 10 and 11 suggests that the initial case velocity $\propto M_0^{-1/2}$.

And figure 12, where the charge size is increased from 1 to 8 kg, with the case thickness of 2.5 mm, contrasts with figure 10 and it is observed that the fragment mass segments attain significantly higher velocities even though the particle diameters are similar to those obtained with a 1 kg charge and 5 mm case thickness as in figure 11. The reason the particle sizes are nearly identical in figure 11 and 12 is seen in figure 9 where the strain rate in these two instances is virtually identical; for the 8 kg charge the case velocity prior to fracture is essentially double that of the 1 kg charge with the heavier case and the initial case radius is also nearly double, hence the same strain rate. The case mass for the 8 kg charge with 2.5 mm thickness is also nearly double that of the 1 kg charge with 5 mm thickness. This then further suggests that the initial case velocity is proportional to $(W / M_0)^{1/2}$.

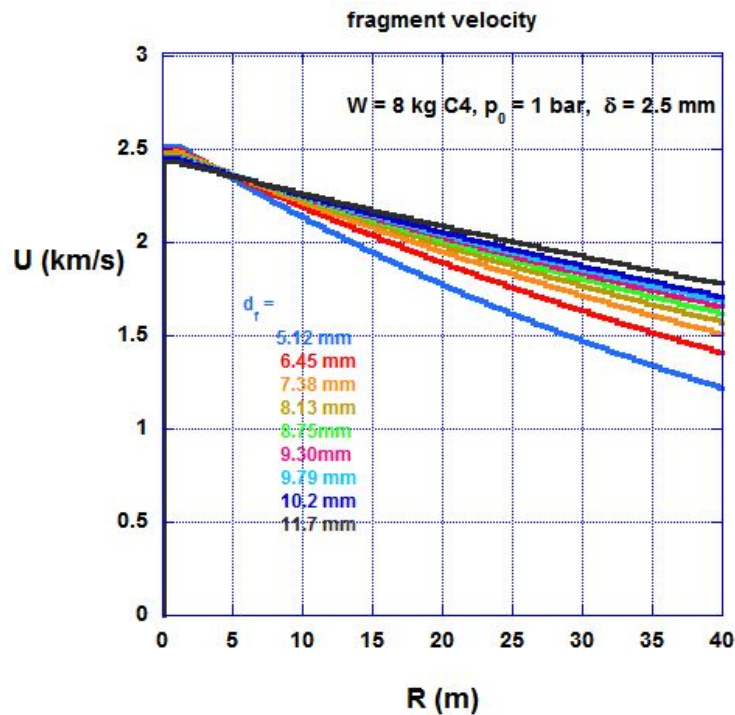


Fig. 12 Fragment velocity for 8 kg charge and 2.5 mm case thickness at sea level.

The fraction of the charge energy coupled to the case prior to fracture is simply $\frac{1}{2}M_0U^2/W$ and study of the results indicates that this quantity attains a maximum value of slightly less than 0.2 when the ratio of the case mass to the mass of the explosive, $\nu = (3\rho/\rho_{ex})\delta/R_0 = 14.71\delta/R_0 = 0.62$ (assuming $\varepsilon_{cr} = 0.05$). For lesser values of ν the coupling efficiency is decreased whereas when this ratio is exceeded $U \approx 0.4\sqrt{W/M_0}$.

3.2 Fragment kinetic energy

Figure 13 shows the ratio of the total kinetic energy imparted to the fragments to the total charge energy as a function of range for the same 4 instances as in figure 9, i.e., the two charge sizes, 1 and 8 kg, and the two case thicknesses, 2.5 mm and 5 mm. In all 4 instances the ambient density (pressure) corresponds to sea level.

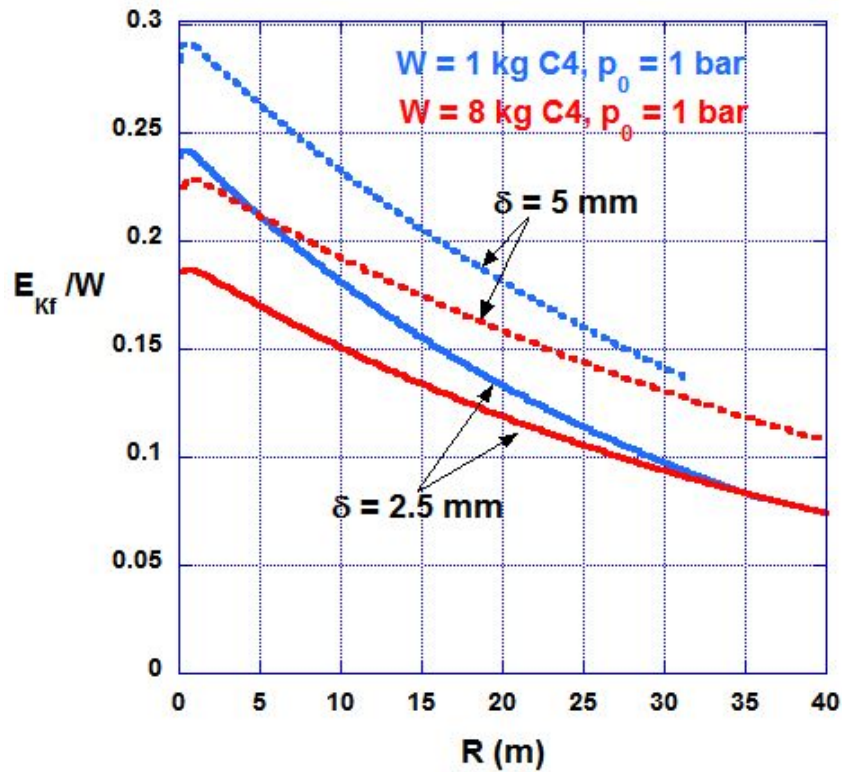


Fig. 13 Fragment kinetic energy ratio at sea level.

It is observed that initial fragment kinetic energy varies with both the yield and the case thickness. For the 1 kg charge, with 5 mm case thickness, 29% of the total charge yield is initially imparted to the fragment ensemble. The number is closer to 19% for the 8kg charge with 2.5 mm case thickness. In all instances the fragment kinetic energy diminishes significantly with range as the fragments are slowed via air drag.

Figure 14 contrasts the situation at sea level with an explosion at an altitude of 30 km, where the ambient air density is reduced by a factor of 64. The kinetic energy ratio is displayed for the 1 kg charge, with 2.5 mm case thickness at both altitudes and it is seen that there is practically no diminution of fragment kinetic energy at the higher altitude. As noted earlier, the reason is simply that the drag force on the fragments, which is directly proportional to the ambient density, is reduced accordingly.

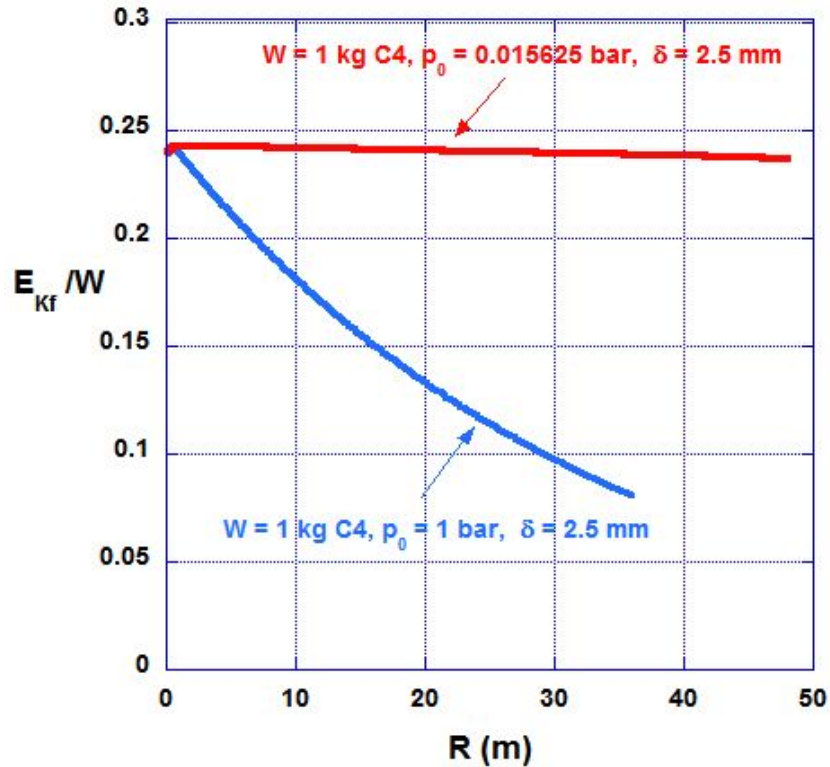


Fig. 14 Comparing fragment kinetic energy at sea level and at 30 km altitude for 1 kg explosion with 2.5 mm case thickness.

3.3 Air blast overpressure and impulse per unit area

Figures 15 and 16 show respectively the overpressure and impulse per unit area as a function of time for the 1 kg charge at sea level, both uncased and with case thicknesses of 2.5 mm and 5 mm, at a range of 1 m; in this case absolute units are used rather than the scaling employed in figure 1. The peak dynamic overpressure for the two cased charges in figure 15 is roughly the same and about 70% that obtained with the uncased charge. Otherwise there is very little difference in the pulse shape. The reason for the lower peak pressure is the energy lost from the air blast that was transmitted to the fragments in the form of kinetic energy. The impulse per unit area, $I = \int (P_{dy} - P_{amb}) dt$, is shown in figure 16 and it is seen that the peak value for the cased charges is about 8% less than for the uncased charge.

Similarly, figure 17 and 18 display the same overpressure and impulse results at a range of 10 m. Here the peak dynamic overpressure is reduced from 1.75 psi for the uncased charge to 1.5 psi for both cased charges. We note that at either level the damage inflicted by such low overpressures would be minimal. For example, from a lethality standpoint, even to inflict significant human hearing loss would require a peak overpressure in excess of 5 psi (*Moor 2007*) so that the most that might be expected at this range would be some discomfort. And again, the decrease in the impulse per unit area for the cased charges,

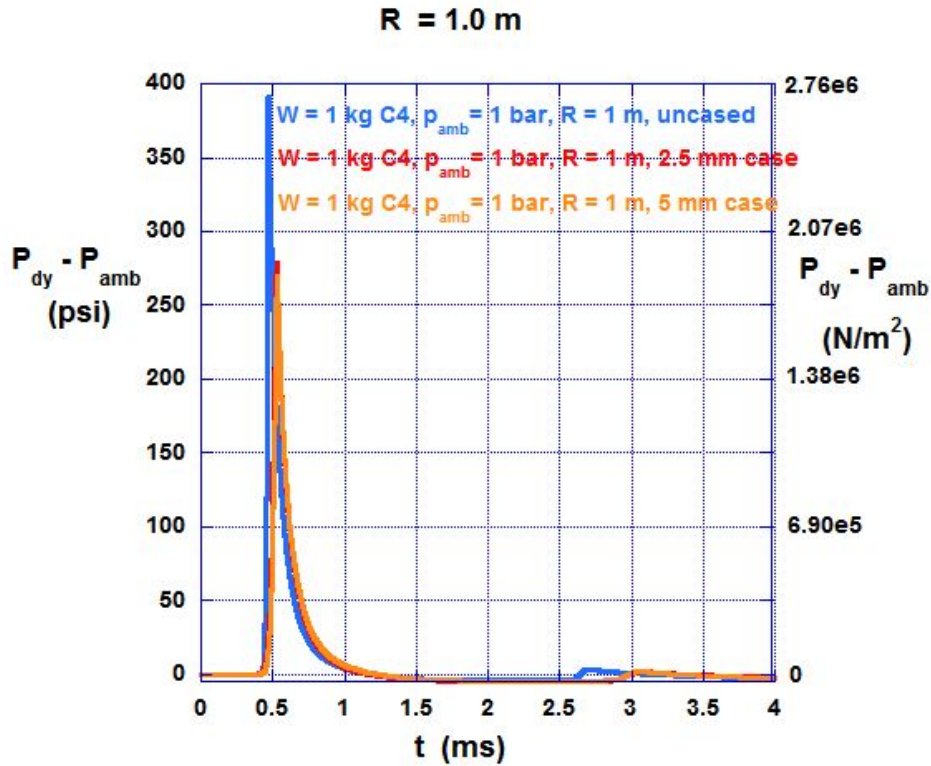


Fig. 15 Dynamic overpressure as a function of time at a range of 1 m.

compared with the uncased charge is about 8%.

Figure 19 through 22 explore the effect of height of burst on the absolute overpressure and impulse per unit area. Since the effect of casing on these quantities has been demonstrated to be minimal we focus here on the uncased charges. Figure 19 displays the peak overpressure at a range of 1 m.

The peak overpressure at 30 km is seen to exceed the value obtained at sea level by about 25% but the pulse is much narrower and the arrival time is considerably earlier. And figure 20 shows that the peak impulse per unit area derived at 30 km is less than half that at sea level.

Figure 21 and 22 display the same overpressure and impulse results at a range of 10 m. The high altitude pulse is seen to be greatly attenuated in comparison to that observed at sea level. The peak overpressure at 30 km is reduced by a factor of 4, to less than 0.4 psi, and the arrival time of the peak is roughly half that at sea level where propagation of the shock is much more efficient through the higher

density air. And figure 22 shows that the impulse per unit area also is reduced by a factor of 4 at the 30 km altitude as compared with that at sea level for the 10 m range.

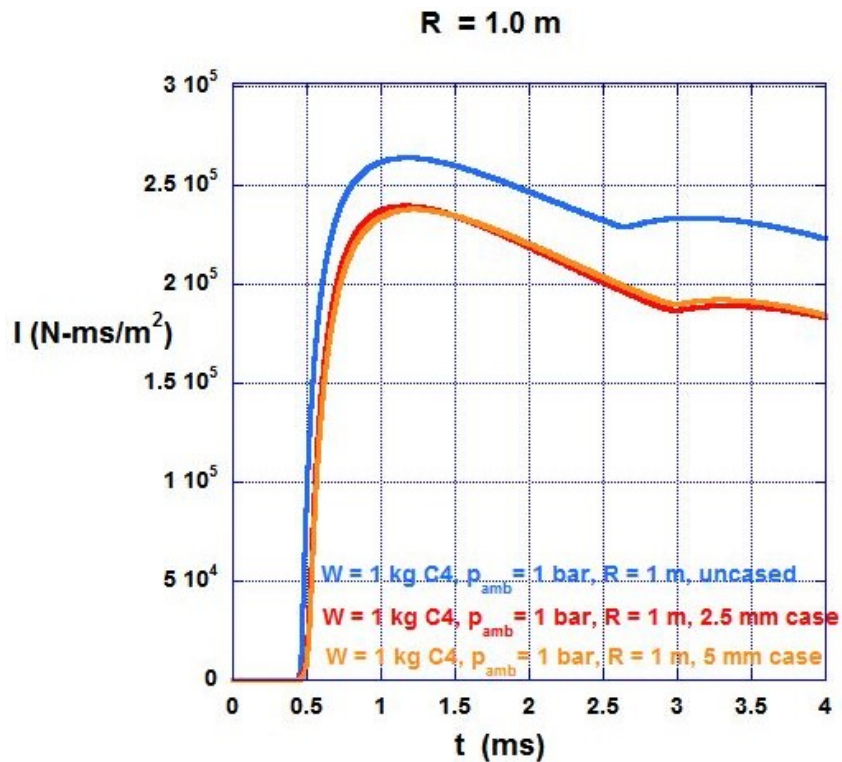


Fig. 16 Impulse per unit area as a function of time at a range of 1 m.

It should be noted that thus far we have been comparing the air blast from only a 1 kg charge, which is consistent with perhaps an anti-personnel weapon. A typical high-altitude mission would involve an aircraft, missile, or re-entry vehicle intercept and, as noted earlier, would typically be with a surface-to-air system like the Patriot whose nominal warhead has an explosive charge of 90 kg. Figure 23 compares the dynamic overpressure produced by a 2.5 mm cased charge of this size at sea level and at 30 km altitude at the nominal 10 m range and figure 24 compares the impulse per unit area at this same range. The peak overpressure is seen to be comparable (28 psi at sea level and 25 psi at altitude) and the peak impulse at sea level is greater by a little more than a factor of 3. In either case the pressure and impulse delivered by such a large charge to an incoming reentry vehicle at this range seems highly likely to at least seriously perturb the trajectory and/or the orientation, quite possibly beyond the possibility for midcourse correction.

However, the dynamic overpressure falls off much more rapidly with range at high altitude than at sea level. Figure 25 re-plots the scaled data from figure 3 in un-scaled coordinates and it is observed that the peak dynamic overpressure at 30 m range has decreased to only 1 psi at 30 km altitude and to 3.3 psi at sea level.

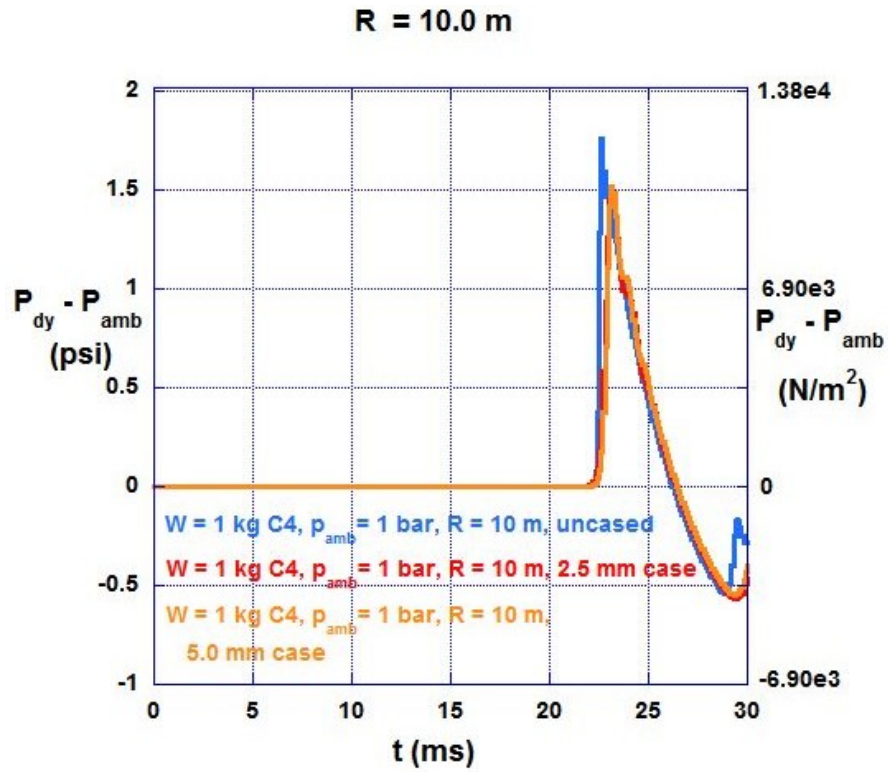


Fig. 17 Dynamic overpressure as a function of time at a range of 10 m.

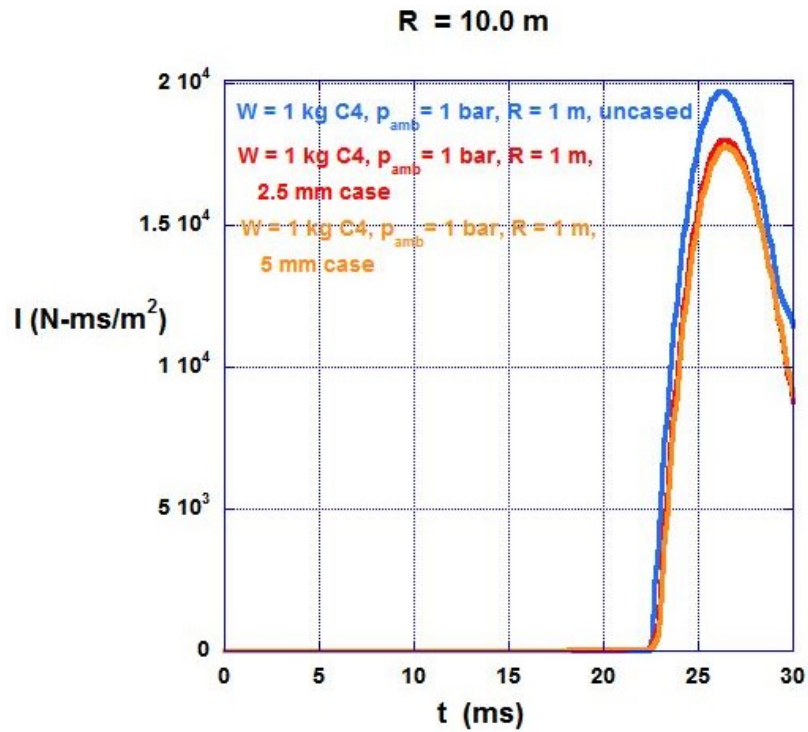


Fig. 18 Impulse per unit area as a function of time at a range of 10 m.

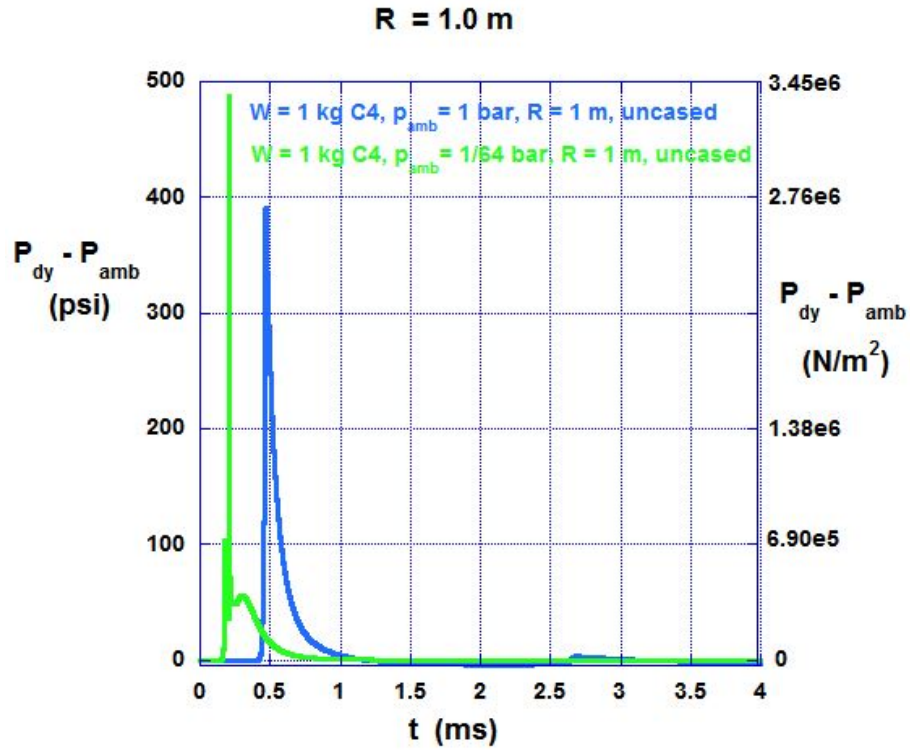


Fig. 19 Comparing dynamic overpressure at sea level and at 30 km altitude for 1 kg uncased explosion at range of 1 m.

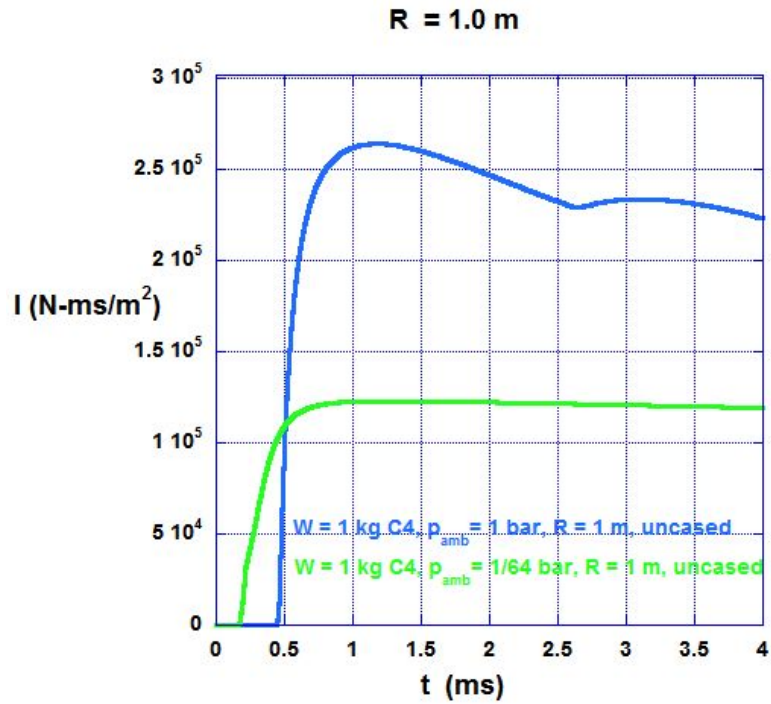


Fig. 20 Comparing impulse per unit area at sea level and at 30 km altitude for 1 kg uncased explosion at a range of 1 m.

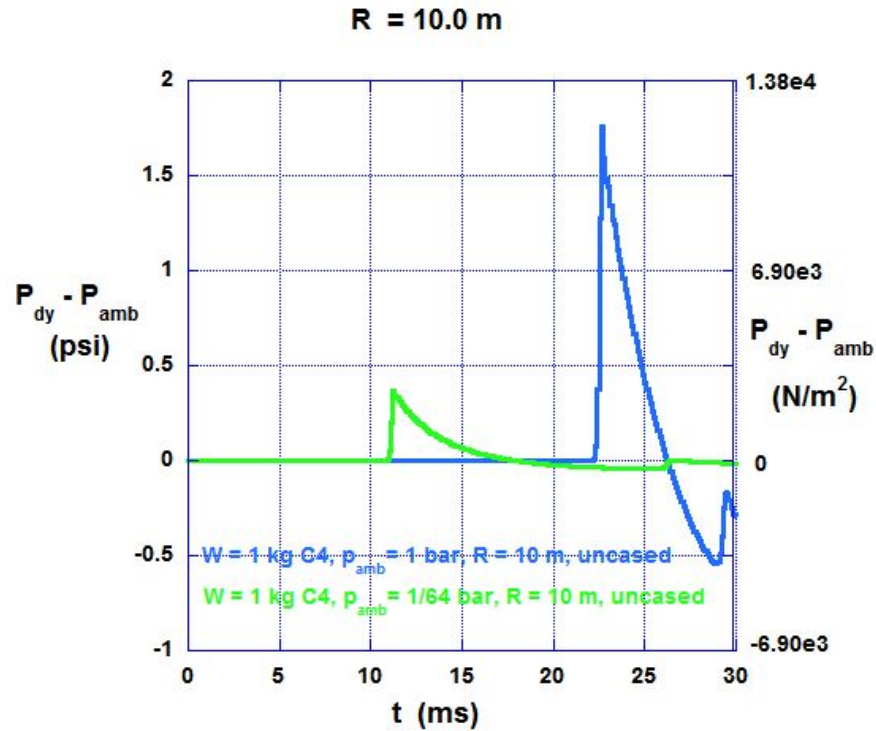


Fig. 21 Comparing dynamic overpressure at sea level and at 30 km altitude for 1 kg uncased explosion at a range of 10 m.

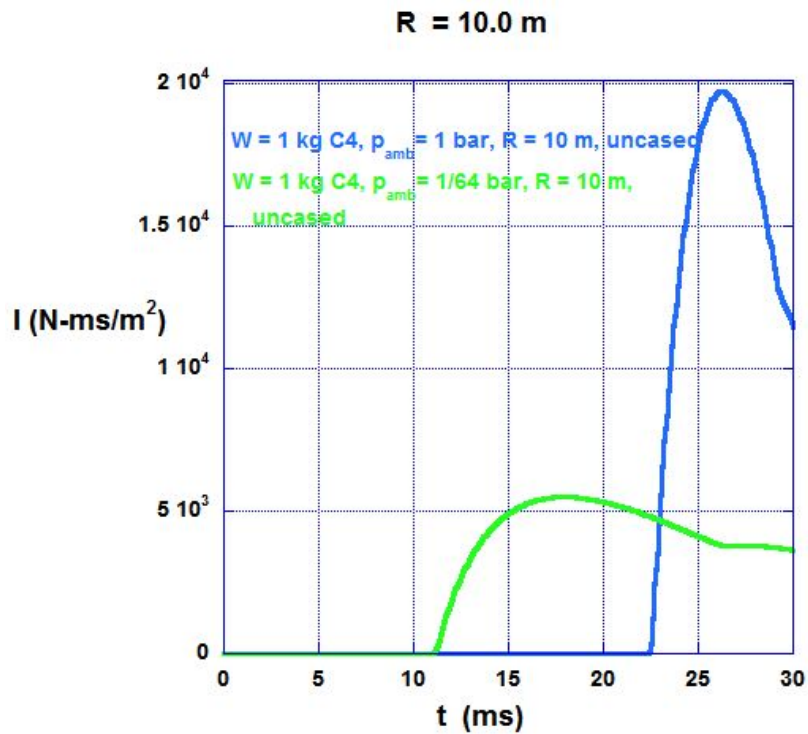


Fig. 22 Comparing impulse per unit area at sea level and at 30 km altitude for 1 kg uncased explosion at a range of 10 m.

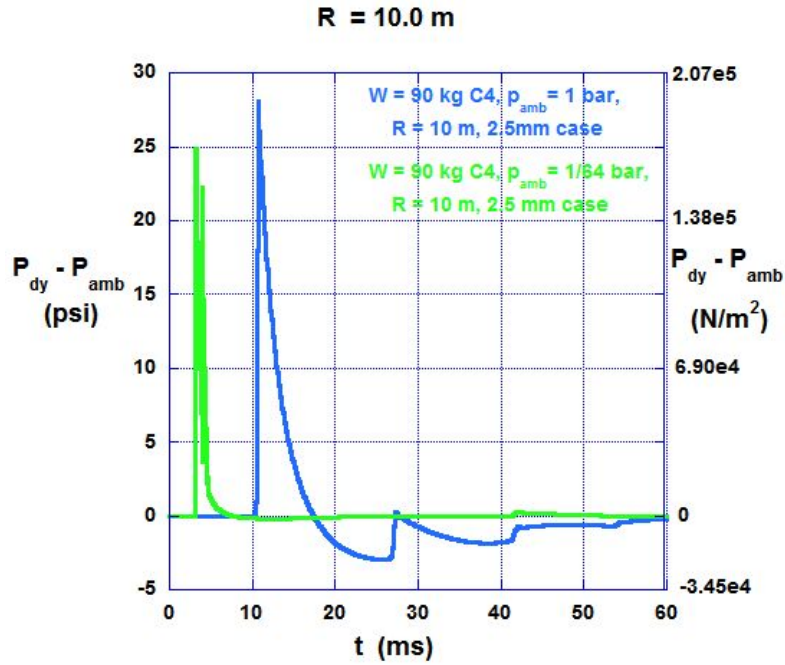


Fig. 23 Comparing dynamic overpressure at sea level and at 30 km altitude for 90 kg, 2.5 mm cased explosion at a range of 10 m.

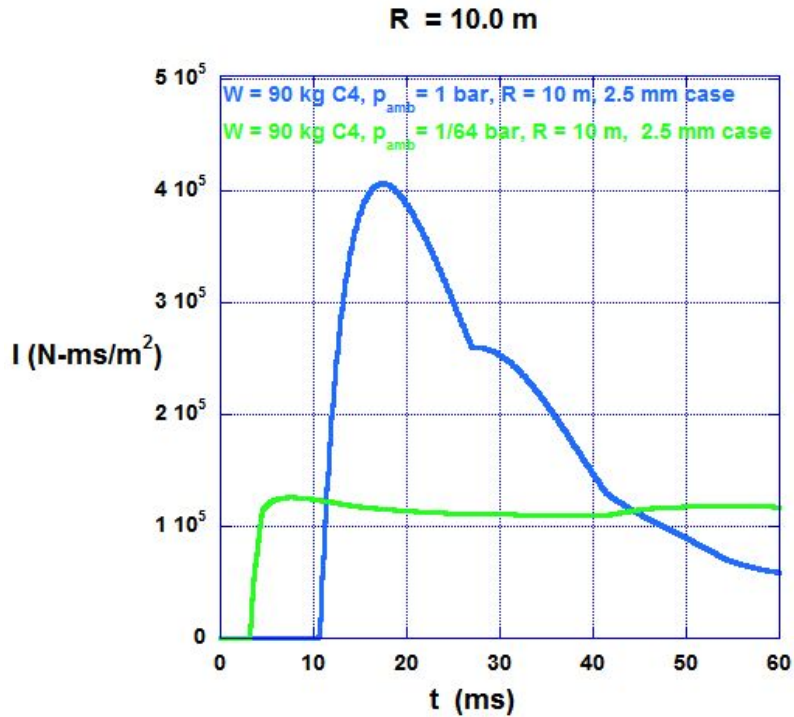


Fig. 24 Comparing impulse per unit area at sea level and at 30 km altitude for 90 kg, 2.5 mm cased explosion at a range of 10 m.

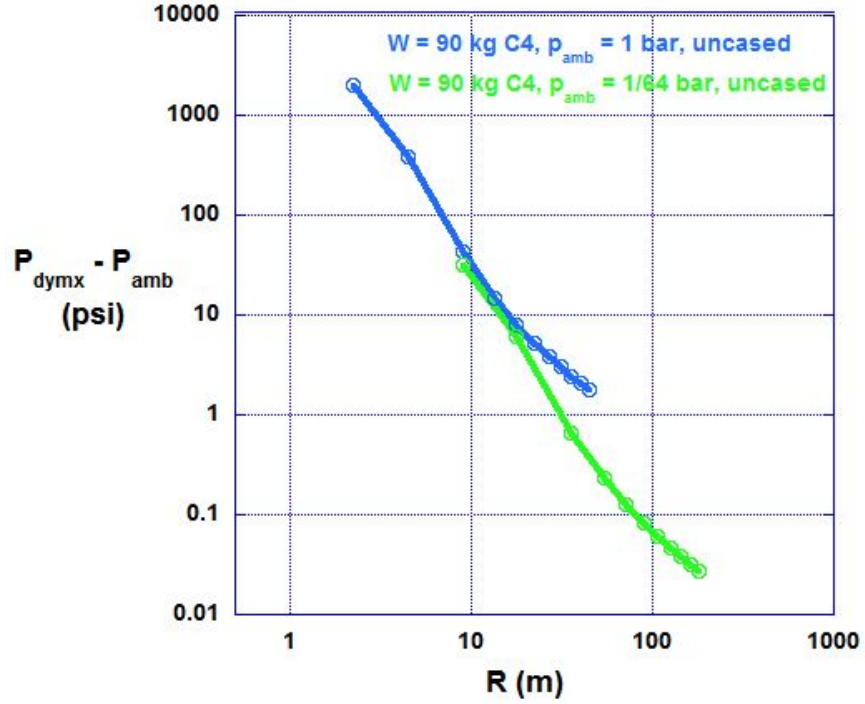


Fig. 25 Peak dynamic overpressure as a function of range for 90 kg uncased explosions at sea level and at 30 km altitude.

3.4 Fragment lethality

The total number of fragments, N_T , produced by a given charge is given by equation (5). Re-writing (5) in terms of \bar{m} ,

$$N_T = \frac{M_0}{\bar{m}} \sum_{k=1}^n \Delta M(k) / \alpha(k) \propto \frac{M_0}{\bar{m}} \propto \frac{R_0^2 \delta}{\bar{m}} \quad (9)$$

where $\Delta M(k)$ is simply the mass fraction of fragments with normalized size $\alpha(k)$. Now

$$\bar{m} \propto \bar{d}_f^3 \propto (\dot{\epsilon}^{-2/3})^3 \propto \dot{\epsilon}^{-2} \quad (10)$$

and, assuming the ratio of the case mass to the mass of the explosive, ν , is at least 0.62,

$$\dot{\epsilon} = \frac{U}{R_0} \propto \frac{(W / M_0)^{1/2}}{R_0} \propto \frac{(R_0^3 / R_0^2 \delta)^{1/2}}{R_0} \propto (R_0 \delta)^{-1/2} \quad (11)$$

Substituting (11) and (10) into (9) yields

$$N_T \propto R_0 \propto W^{1/3} \quad (12)$$

so that, for heavy enough case mass, the total number of fragments scales with the cube root of the yield. If $\nu < 0.62$ N_T will be somewhat less than predicted by (12).

Figure 26 displays the total number of fragments per unit area assuming the fragments are uniformly distributed over 4π steradians.

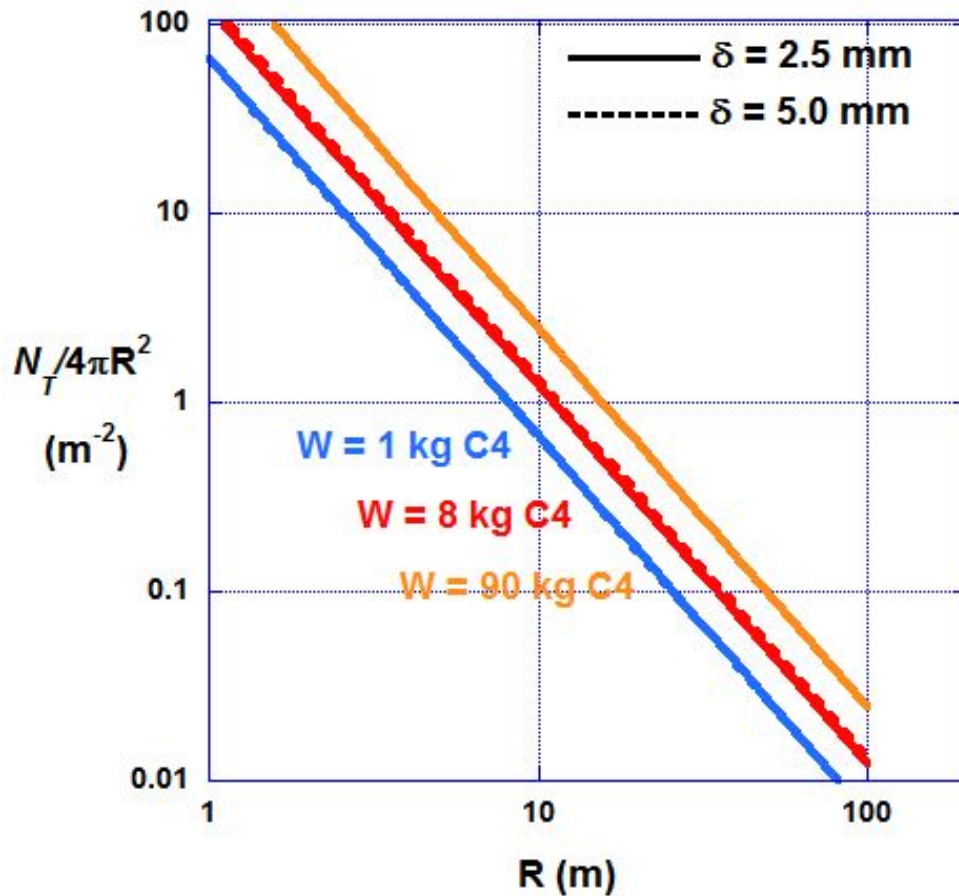


Fig. 26 Areal density of fragments as a function of range, charge size and case thickness.

The areal density is independent of altitude, although not the velocity of the fragments which, as was seen above, increases with increasing altitude. For the 1 kg charge the number of fragments per unit area appears independent of case thickness because $\nu \geq 0.62$ for both 2.5 mm and 5mm case thicknesses. For the 8 kg charge a slight difference can be seen for the 2 case thicknesses. And for the 90 kg charge only the results for the 2.5 mm thick case are shown because the heavier cases resulted in average fragment sizes that were less than the Griffith limit (figure 8) and might not be realistic for 4340 steel.

We note that, at a range of 10 m, the areal density for the 1kg charge is 0.66 m^{-2} and 1.33 m^{-2} for the 8 kg charge, which agrees fairly well with the cube root yield scaling described above. The 90 kg charge, on the other hand, exhibits an areal density of only 2.6 m^{-2} , which is somewhat less than the 2.96 number that would result from cube-root-yield scaling. In all cases, however, the areal density at this range would likely result in target collisions with at least one fragment. If the target were a reentry vehicle, with incoming velocity in the 6-7 km/s range, the impact would be explosive and the effect on the vehicle likely quite deleterious.

Finally, it should be pointed out that the areal density shown in figure 26 is a minimum in that it is possible to design a warhead wherein the fragments are distributed over significantly less than 4π steradians. And it is also possible to embed inert fragments in the explosive charge itself, thereby increasing the fragment number even further.

4.0 Summary

For an unconfined (uncased) chemical explosive, both range and time to effect scale inversely as the cube root of the yield and directly as the cube root of the ambient air density. The peak overpressure decays to roughly 1/10 of ambient pressure in a scaled range of roughly $10 \text{ m/kg}^{1/3}$ at sea level. At a height of 30 km, where the ambient density is a factor of 64 less, the range to the same decay increases to $40 \text{ m/kg}^{1/3}$. As a direct result of the scaling a single calculation suffices for all charge sizes and altitudes. Although the close-in results are extremely sensitive to the nature of the explosive source and the equation of state of the air, this sensitivity is shown to virtually disappear at scaled ranges $> 0.5 \text{ m/kg}^{1/3}$.

For cased explosives, the case surrounding the charge shatters and carries away a significant fraction of the total yield in the form of fragment kinetic energy. A model of the fragmentation process, and the subsequent motion of the fragments, was implemented in the STUN code, and a series of calculations was carried out to determine the effects of case thickness, charge size and ambient density (altitude) on the air blast overpressure and on the areal density of fragments.

Although detailed damage estimates are beyond the scope of the present study some qualitative observations can be made. For small (anti-personnel) charges the air blast quickly decays with range so that, at a range of 10 m, the likely damage is minimal. However, at this range, the fragment areal density is still sufficient to likely be gravely damaging. For larger charges, that are employed in surface to air missiles for example, the air blast at 10 m range, even at 30 km altitude, is likely to seriously perturb the trajectory and/or the orientation of the target and the fragment areal density would be expected to cause serious target damage.

References

Bethe, H. A., Shock hydrodynamics and blast waves, Los Alamos Report AECD-2860, October 28, 1944, pp 52-62.

Brode, H. I., Numerical solution of spherical blast waves, *J. Appl. Phys.*, **26**, 766 (1955).

Brode, H. I., Point source explosion in air, RAND Corporation Research Memorandum RM-1824-AEC, December 3, 1956 (ASTIA Document Number AD 133030).

Elek, P. and Jaramaz, S., Size distribution of fragments generated by detonation of fragmenting warheads, 23rd International Symposium on Ballistics, Tarragona, Spain, 16-20 April 2007.

Glenn, L. A., Simulating MARVEL with the STUN code, Lawrence Livermore National Laboratory UCRL-ID-143993, June 6, 2001.

Glenn, L. A., Gommerstadt, B. Y., and Chudnovsky, A., A fracture mechanics model of fragmentation, *J. Appl. Phys.*, **60**, 1224 (1986).

Glenn, L. A. and Chudnovsky, A., Strain-energy effects on dynamic fragmentation, *J. Appl. Phys.*, **59**, 1379 (1986).

Glenn, L. A. and Lomov, I. N., A simple model for the explosive dispersal of metal powders, Lawrence Livermore National Laboratory UCRL-TR-583772, September 21, 2012.

Grady, D. E. and Kipp, M. E., Geometric statistics and dynamic fragmentation, *J. Appl. Phys.*, **58**, 1210 (1985).

Lee, E. L., Hornig, H. C. and Kury, J. W., Adiabatic expansion of high explosive detonation products, University of California Report UCRL-50422, 1968.

Moor, E. H., Engineering design safety manual section 4.1, personnel and equipment shields, UCRL-TM-229115, Lawrence Livermore Laboratory, Livermore, CA (2007).

Mott, N. F., A theory of fragmentation, British Ministry of Supply Reports, 3348, 3642, 4035 (1943).

von Neumann, J., Shock hydrodynamics and blast waves, Los Alamos Report AECD-2860, October 28, 1944, pp 48-52.

Reimer, R. J. and Rogers, H. C., Dynamic fracture phenomena in high-strength steels, *J. Appl. Phys.*, **50**, 8025 (1979).

Ripley, R. C., Acceleration and heating of metal particles in condensed matter detonation, Doctoral dissertation, University of Waterloo, Waterloo, Ontario, Canada (2010).

Ritchie, R. O., Francis, B., and Server, W. L., Evaluation of toughness in AISI 4340 alloy steel austenized at low and high temperature, *Met. Trans. A*, **7A**, 831 (1976).

Smirnov, N., N., Combustion and detonation in multi-phase media; initiation of detonation in dispersed-film systems behind a shock wave, *Int. J. Heat Mass Transfer*, **31**, 779 (1988).